

A Two-body Rigid/Flexible Model of Needle Steering Dynamics in Soft Tissue

Mohsen Khadem¹, Carlos Rossa¹, Nawaid Usmani², Ron S. Sloboda², Mahdi Tavakoli¹

Abstract—Robotics-assisted needle steering can enhance targeting accuracy in percutaneous interventions. This paper presents a novel dynamical model for robotically controlled needle steering. This is the first model that predicts both needle shape and tip position in soft tissue and accepts needle insertion velocity, needle 180° axial rotation, and needle base force/torque as inputs. A hybrid formulation of needle steering dynamics in soft tissue is presented, which considers the needle as a two-body rigid/flexible coupled system composed of a moving, discrete and rigid part attached to a vibrating compliant part that is subject to external excitation forces. The former is the carrier representing the surgeon’s hand or the needle inserting robot while the latter is a beam modeling the continuous deflection of the needle inside tissue. A novel time-delayed tissue model and a fracture mechanics-based model are developed to model the tissue reaction forces and cutting force at the needle tip, respectively. Experiments are performed on synthetic and ex-vivo animal tissues to identify the model parameters and validate the needle steering model. The maximum error of the 2D model in predicting the needle tip position in the insertion plane was 1.59 mm in case of no axial rotation and 0.74 mm with axial rotation.

Index Terms—Medical robotics, Needle steering, Dynamic modeling

NOMENCLATURE

$XY,xy,\xi\eta$	Global inertial frame, carrier Body-fixed frame, and needle Body-fixed frame.
t	Time.
N	Generic point on the deflected needle.
N_0	Point N on the unbent needle.
$R_N(x, t)$	Vector of coordinates of point N .
$R^G(t)$	Vector of coordinates of needle-carrier center of mass.
$r(x)$	Vector of coordinates of N_0 .
$u(x, t)$	Displacement vector connecting N_0 to N .
$C(t)$	Matrix of direction cosines.
$X(t),Y(t)$	Displacement of carrier along X and Y axes.
$\theta(t)$	In-plane angle of rotation of carrier.
$\Theta(t)$	Vector of carrier Euler angles.
$u(x, t)$	Displacement of point N along x axis.
$\omega(x, t)$	Displacement of point N along y axis.
$\psi(x, t)$	In-plane angle of rotation of point N .
$\psi(x, t)$	Vector of point N Euler angles.
$V(t)$	Velocity vector of the carrier center of mass.
$\dot{\theta}(t)$	Angular velocity of xy relative to XY .
$\dot{u}(x, t)$	Elastic velocity vector.
$\dot{\psi}(x, t)$	Elastic angular velocity of $\xi\eta$ frame.
\mathbf{I}	9×9 identity matrix.
$V_N(x, t)$	Velocity vector of point N of needle.
ζ	Dummy integral variable.
\mathcal{L}	Lagrangian.
$T(t),\mathcal{V}(t)$	Kinetic and potential energy of needle-carrier system.
$\delta\mathcal{W}(t)$	Virtual work.
$\delta(\cdot)$	Infinitesimal variation operator.
ℓ, A, I, α	Needle’s length, cross-section area, second moment of inertia, and bevel angle.
ρ, E	Needle’s density and Young’s modulus.
m_c, \mathbf{J}_c	Carrier’s mass and moment of inertia.

*Correspondence: Mohsen Khadem, Department of Electrical & Computer Engineering, University of Alberta, Edmonton, AB, Canada, T6G 2V4, Email: mohsen.khadem@ualberta.ca, Phone: +1-780-2007829.

¹M. Khadem, C. Rossa, and M. Tavakoli are with the Department of Electrical and Computer Engineering, University of Alberta. {mohsen.khadem, rossa, mahdi.tavakoli}@ualberta.ca

²R. S. Sloboda, PhD, FCCPM, and N. Usmani, MD, are with the Cross Cancer Institute and the Department of Oncology, University of Alberta. {ron.sloboda, nawaid.usmani}@albertahealthservices.ca

m_t, \mathbf{J}_t	Needle-carrier system’s total mass and total moment of inertia.
\mathbf{g}	Vector of gravitational field strength.
$\mathbf{F}_c(t)$	Vector of forces acting on the carrier.
$\mathbf{F}_{cx}(t)$	Forces acting on the carrier along x axis.
$\mathbf{F}_{cy}(t)$	Forces acting on the carrier along y axis.
$\mathbf{M}_c(t)$	Vector of torques acting on the carrier.
$M_{cz}(t)$	In-plane torque acting on the carrier.
$f(x, t)$	Vector of distributed interaction forces on needle shaft.
$f_x(x, t)$	Distributed interaction forces along x axis.
$f_y(x, t)$	Distributed interaction forces along y axis.
$F_s(x, t)$	Soft-tissue reaction force.
$F_f(x, t)$	Needle-tissue friction force.
$F_c(t)$	Tissue cutting force.
$F_{c\xi}(t)$	Axial and transverse cutting forces along ξ axis.
$F_{c\eta}(t)$	Axial and transverse cutting forces along η axis.
K_t, l_t, d_t	Template’s stiffness, length, and distance from the tissue.
$x_t(t)$	Position of the template in xy .
H, δ	Unit step and Dirac delta functions.
$W_i(x)$	Assumed mode shapes of vibration, $i = 1, \dots, n$.
n	Number of assumed modes.
$\phi_i(t)$	Generalized coordinate, $i = 1, \dots, n$.
β_i	Vibration frequency constant, $i = 1, \dots, n$.
γ_i, κ_i	Vibration amplitude constants, $i = 1, \dots, n$.
$\phi(t), \mathbf{W}(x)$	Vectors of generalized coordinates and mode shapes.
G_c	Fracture toughness.
$G(t)$	Crack extension energy release rate.
ν	Poisson’s ratio.
K_I	Stress intensity factor for mode I fracture.
A	Universal function of crack speed.
$K_{ID}(t)$	Dynamic stress intensity factor for mode I fracture.
c_r	Raleigh surface wave speed.
h, m	Dynamic crack extension constants.
K_{I0}	Dynamic stress intensity at zero velocity.
V_l	Limiting crack speed.
w_c	Width of cutting.
K_s, C_s	Tissue stiffness and damping coefficient per unit length of needle.
τ	Tissue model delay.
φ_{ij}, χ_{ij}	Tissue model state variables, $i, j = 1, \dots, n$.

I. INTRODUCTION

Needle-based interventions are common minimally invasive medical procedures. An example is prostate brachytherapy, where a flexible needle passing through a grid template is inserted in tissue, such that radioactive sources loaded in the needles can be placed in or near the tumor. Robotics-assisted needle insertion can increase percutaneous medical procedures efficiency, which highly depends on accurate control of the needle tip trajectory. Modeling the needle deflection and the interaction between needle and soft tissue is an essential requirement for robotic needle steering and surgical planning and has been the topic of significant research efforts [1]–[3]. Here, a novel hybrid model of needle-tissue interaction is presented. The hybrid modeling implies mixed use of ordinary differential equations (ODE) to model the surgeon’s hand and/or a rigid needle carrier, as well as continuous partial differential equations (PDE) to model the needle-tissue interaction. The proposed model can be used for needle steering in robotic-assisted needle insertion schemes.

A. Related Work

Modeling of needle-tissue interaction makes it possible to steer flexible needles from outside the body to reach specified targets inside the body. The term *steering* implies control of

the needle tip deflection and changing the direction of the needle tip trajectory as the needle is being inserted by means of inputs such as axial rotation, lateral manipulation, and insertion velocity control of the needle base. A needle steering model predicts the needle trajectory inside tissue based on the aforementioned steering inputs. DiMaio and Salcudean [4], and Goksel *et al.* [5] are among the first researchers who used the Finite Element Method (FEM) to model the needle/tissue interaction in order to find the needle tip position. Alterovitz *et al.* presented a 2D FEM model of needle insertion considering the effect of the tip bevel [6]. Chentanez *et al.* expanded the model into 3D [7]. Park *et al.* developed a simple nonholonomic unicycle model to describe how an ideal needle with bevel tip moves through firm tissue [8]. Webster *et al.* extended this idea and developed a nonholonomic bicycle-like model for steering flexible bevel-tipped needles [3]. The model assumes that the needle tip trajectory has a constant radius of curvature and follows a circular path.

Several research groups have used classical beam theories to develop fundamental mechanics-based models [2], [9], [10]. Misra *et al.* used an energy-based formulation for a beam that is in contact with a nonlinear hyperplastic tissue to simulate needle steering [2]. This model accounts for lateral and axial deflection of the needle, tissue deformation, and input force applied at the needle base. Later, the same model was extended to include needle rotation during needle insertion [11]. From our group, Khadem *et al.* used a dynamic beam theory to study the effects of insertion velocity on needle deflection [12]. In the proposed model, tissue cutting force and tissue deformation was assumed to be velocity-independent and a uniform force profile was used to model tissue reaction force. Also, the effect of needle axial rotation on needle deflection and tissue deformation was not studied. Reed *et al.* studied effects of torsional friction on needle deflection dynamics [13]. They developed an estimator showed that the estimator allows the needle to maintain motion in a prescribed plane. Swensen *et al.* also investigated the torsional dynamics of the needle modelled as a beam and developed a model-based controller that compensates for the changing boundary conditions during subsurface needle insertion [1].

Design of needle steering planners and most types of feedback controllers requires a model of needle-tissue interaction that predicts the needle tip position given the inputs at the needle base such as insertion velocity and needle axial rotation. In the preceding models, a common approach for simulating needle deflection is using FEM [4], [6]. Employing a comprehensive FEM model of tissue can be very time-consuming – more time-efficient ways to model tissue come at the expense of reduced accuracy [5]. Also, some of the preceding models do not present sufficient control commands for real-time feedback control, which limits their application in real-time needle steering [1], [2], [10].

To the best of the authors' knowledge, the nonholonomic kinematics-based models [3], [8] are the only model that has insertion velocity and axial needle rotation as inputs. The kinematics-based model has been widely used for robotic needle steering [14]–[16]. The model does not account for needle-tissue interaction along the needle shaft and assumes the needle tip moves on a constant curvature path. Previous studies have shown that when the kinematic model is applied to path planning and control in soft tissues, there are non-

negligible deviations between the model and experimental data [17]. In summary, various inputs such as insertion velocity and axial rotation can be used for needle steering. A dynamic or kinematic model is needed to relate these inputs to the system states (needle shape) and output (needle tip position). In this paper, we have developed a novel model of needle steering that accepts insertion velocity, axial rotation, and needle base force/torque as inputs and can be used for robotics-assisted needle steering.

B. Contributions

In the current work, a hybrid approach is used to model needle steering in soft tissue. Our hybrid ODE/PDE model is inspired by spacecraft dynamics literature where such models are used to investigate the dynamics of multi-body systems composed of a moving, discrete and rigid part attached to a vibrating compliant part. Here, a computationally efficient needle steering model is developed that allows for real-time control of needle tip position in a robotic-assisted needle insertion scheme. Other contributions of this paper include: (1) A novel *time-delayed* tissue model that enables modeling of needle axial rotation during needle insertion. (2) The needle steering model explicitly relates needle deflection to the insertion velocity, insertion force/torque, and axial rotation of needle; therefore, these parameters can all be used as control commands for closed-loop needle steering.

This paper is organized as follows: In Section II, details of the needle steering model including the modeling assumptions, kinematic and dynamic modeling, and model simplification are presented. In Section III, separate complementary models are developed to simulate interaction forces between the needle and its surrounding environment. In Section IV, the needle steering model is validated through intensive needle insertion experiments on synthetic and ex-vivo animal tissues and results of the experiments are discussed. Concluding remarks are presented in Section V.

II. MODELING: TWO-BODY RIGID/FLEXIBLE DYNAMICS

In this paper needle deflection is modelled as externally excited compliant beam attached to a rigid carrier. The elastic needle is modelled as a prismatic beam that deflects under various external forces, i.e., reaction forces from deformed soft tissue, needle-tissue friction, the grid template contact force, and tissue cutting force. Template grids consist of rows and columns of holes providing guidance for accurate placement of radioactive seeds in predefined locations of the prostate (see Fig. 1(a)). The carrier has two translational and one rotational degrees of freedom (DoF). The carrier can be a physical component (e.g., the surgeon's hand or the needle inserting robot) or may simply be a virtual massless body with a body-fixed frame. Fig. 1 shows a schematic diagram of the needle insertion system.

An advantage of the proposed modeling technique is that we can explicitly see the effects of the forces and torques applied to the carrier on needle deflection, and vice versa. These forces and torques are usually recorded during robotic needle insertions. By relating them to the needle deflection using the proposed model they can be used as feedback or control inputs in a robotically controlled needle steering.

The following assumptions are used in modeling the needle deflection during insertion into the tissue:

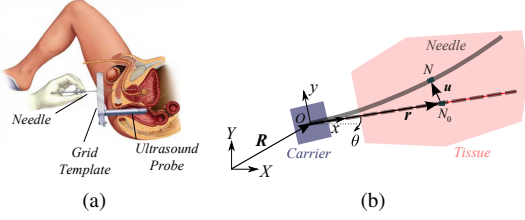


Fig. 1. Needle insertion in brachytherapy. (a) shows the surgeon inserting the flexible needle in the tissue. (b) shows a sketch of the needle insertion system consisting of a flexible needle attached to a rigid carrier.

(1) The needle has only 2D planar deflection and the insertion plane is defined by initial orientation of the needle beveled tip. (2) The needle is modelled as homogeneous beam with constant cross section area that is infinitely stiff in shear. (3) Planar rotation of beam elements is small and rotary inertia of the needle due to needle bending is negligible. (4) The axis of the prismatic beam is incompressible and needle shortening due to axial compression is neglected. However, axial forces can affect needle bending dynamics when the deflection is large. (5) The center of mass of the needle driving system is assumed to coincide with that of the carrier. Thus, the potential energy of the needle-tissue system is only due to the needle flexibility and the mass of the carrier.

Assumptions 2 and 3 are Euler-Bernoulli beam theory assumptions [18], which hold as long as the ratio of the beam height to the radius of curvature of the beam is much smaller than unity which is the case for all brachytherapy needles. During needle steering, the needle tip might deviate and deflect out of plane. However, using the process presented in [13] and [1] we can minimize the out of plane deflection and maintain a 2D needle insertion.

In the following, the generalized coordinates and kinematics of the needle-tissue system are introduced. Next, we use the variational formulation to model the dynamic motion of the needle inside the tissue. Finally, a mathematical approach is used to simplify the dynamic equations. Throughout this paper we use the following notation: s , \mathbf{s} and \mathbf{s} denote a scalar, a vector and a matrix, respectively.

A. Kinematics of Needle Steering

Fig. 1(b) shows a schematic diagram of the needle insertion system. A global inertial frame (XY) and a non-inertial frame (xy) fixed on the carrier at its mass center are defined. The generic point N_0 along the needle shaft when the needle is unbent coincides with the point N when the needle is deflected. The coordinates of point N of the deflected needle in the body-fixed frame is

$$\mathbf{R}_N = \mathbf{C}\mathbf{R}^G + \mathbf{r} + \mathbf{u} \quad (1)$$

where $\mathbf{R}^G = [X \ Y \ 0]^T$ is expressed in coordinates of the inertial frame, $\mathbf{r} = [x \ 0 \ 0]^T$, $\mathbf{u} = [u \ \omega \ 0]^T$, and $\mathbf{C} = \begin{bmatrix} \cos(\theta) & \sin(\theta) & 0 \\ -\sin(\theta) & \cos(\theta) & 0 \\ 0 & 0 & 1 \end{bmatrix}$. \mathbf{C} allows to transform a point from (XY) frame to (xy) frame. Note that \cdot^G indicates a vector defined in the global inertial frame and vectors with no superscript are all in terms of the body-fixed frame coordinates.

It should be emphasized that in our approach all the forces and torques applied to the needle and carrier are defined with respect to the non-inertial frame attached to the carrier called the *body-fixed frame*. Thus, it is more convenient to define our generalized coordinates and velocities in the body-fixed frame

– they are customarily referred to as pseudo-coordinates and pseudo-velocities, respectively [19].

The carrier has two translational DoF along X and Y , denoted by the vector \mathbf{R}^G . In addition to two translational DoFs, the carrier has a rotational DoF, θ , denoted by the vector of Eulerian-type angles $\boldsymbol{\theta} = [0 \ 0 \ \theta]^T$. According to the Assumption 1, the first two angles are zero. Point N on the needle has three DoFs in the body-fixed frame, namely ω , u and ψ , corresponding to displacements along x and y and the in-plane rotation, respectively (see Fig. 2).

To model in-plane rotational motion of beam elements, we introduce a set of body-fixed frames ($\xi\eta$) attached to the cross-section of the beam at point N . Denoting the in-plane bending rotation of beam element by ψ and assuming it is small, we can express rotation of the $\xi\eta$ frame relative to the xy frame by the vector $\boldsymbol{\psi} = [0 \ 0 \ \psi]^T$.

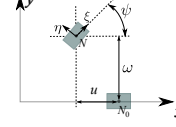


Fig. 2. Needle element bending displacement.

Based on the presented configuration of the needle-carrier system we have the vector of generalized coordinates $\mathbf{q} = [\mathbf{R}^{G^T} \ \boldsymbol{\theta}^T \ \mathbf{u}^T \ \boldsymbol{\psi}^T]^T$. Now, we can easily calculate the generalized velocities related to the derivatives of the generalized coordinates by

$$[\mathbf{V}^T \ \dot{\boldsymbol{\theta}}^T \ \dot{\mathbf{u}}^T \ \dot{\boldsymbol{\psi}}^T]^T = \begin{bmatrix} \mathbf{C} & 0 \\ 0 & \mathbf{I} \end{bmatrix} \dot{\mathbf{q}} \quad (2)$$

All vectors in (2) are in body-fixed frame (xy). Now taking derivative of (1) with respect to time, we can write the kinematic equation of motion for point N in terms of generalized velocities as

$$\mathbf{V}_N = \mathbf{V} + \tilde{\boldsymbol{\theta}}(\mathbf{u} + \mathbf{r}) + \dot{\mathbf{u}} = \mathbf{V} + (\tilde{\mathbf{u}}^T + \tilde{\mathbf{r}}^T)\dot{\boldsymbol{\theta}} + \dot{\mathbf{u}} \quad (3)$$

the superscript \sim denotes a skew symmetric matrix.

At this point, we introduce two equations that can be used to eliminate the redundant coordinates. Using Euler-Bernoulli assumptions we have

$$u(x, t) = -\frac{1}{2} \int_o^x \omega'(\zeta, t)^2 d\zeta \quad (4a)$$

$$\psi(x, t) = \omega'(x, t) \quad (4b)$$

where prime denotes partial derivative with respect to x . Above equations will be used later to write ψ and u in terms of other generalized coordinates and eliminate redundant degrees of freedom.

B. Variational Formulation of Needle Steering

Having all the kinematic equations that describe the motion of the needle and the carrier, we will use the variational formulation and extended Hamilton's principle to derive the dynamic equations of motion for the hybrid system. We note that \mathbf{V} in (3) is defined in the body-fixed frame and based on (2), the components of \mathbf{V} are not direct derivatives of generalized coordinates. \mathbf{V} is typically called the derivative of pseudo-coordinates or pseudo-velocity vector. Similar to velocity, it is simpler to define all the forces and torques applied to the carrier and needle with reference to the body-fixed frame. Thus, it is more convenient to use the extended

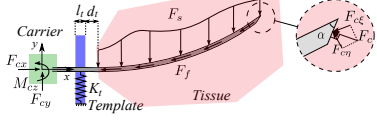


Fig. 3. Interaction forces acting on the length of the bevel-tip needle inserted into a soft tissue.

Hamilton's principle in terms of pseudo-coordinates. The extended Hamilton's principle stated by

$$\int_{t_1}^{t_2} [\delta \mathcal{L} + \bar{\delta} \mathcal{W}] dt = 0 \quad (5)$$

Before we can use (5), it is essential to find the expressions for T , \mathcal{V} , and $\bar{\delta} \mathcal{W}$.

Based on Assumption 3, the kinetic energy consists of only three parts, one due to the translation of an element of mass associated with the cross-sectional area of beam at a nominal position x , one due to the translation of the carrier, and one due to the rotation of the carrier. Using (3), we can write the kinetic energy as

$$T = \frac{1}{2} \rho A \int_o^l [\dot{\mathbf{u}}^T \dot{\mathbf{u}} + 2 \mathbf{V}^T \dot{\mathbf{u}} + 2 \mathbf{V}^T (\tilde{\mathbf{u}}^T + \tilde{\mathbf{r}}^T) \dot{\theta} + 2 \dot{\theta}^T (\tilde{\mathbf{u}} + \tilde{\mathbf{r}}) \dot{\mathbf{u}}] dx + \frac{1}{2} m_t \mathbf{V}^T \mathbf{V} + \frac{1}{2} \dot{\theta}^T \mathbf{J}_t \dot{\theta} \quad (6)$$

where $\mathbf{J}_t = \mathbf{J}_c + \rho A \int_o^l (\tilde{\mathbf{u}} + \tilde{\mathbf{r}})^T (\tilde{\mathbf{u}} + \tilde{\mathbf{r}}) dx$ and $m_t = m_c + \rho A l$ is the total mass of the needle-carrier system.

The potential energy of the system arises from two sources, gravity and needle flexibility. Considering Assumption 5, the gravitational potential energy of the needle is negligible. Also, from mechanics of materials, the bending potential energy of the deflected needle is equal to $\frac{1}{2} EI \int_o^l \psi'^2 dx$ [18]. Replacing ψ using the kinematic constraint given by (4b), the total potential energy can be expressed as

$$\mathcal{V} = -m_c \mathbf{g}^T \mathbf{R} + \frac{1}{2} EI \int_o^l \omega''^2 dx \quad (7)$$

The non-conservative virtual work is due to the forces and torques applied to the carrier and a distributed force working on the length of the flexible needle. It can be written as

$$\bar{\delta} \mathcal{W} = \delta \theta^T \mathbf{M}_c + \delta \mathbf{R}^T \mathbf{C}^T \mathbf{F}_c + \int_0^l \delta \mathbf{R}_N^T \mathbf{f} dx \quad (8)$$

where $\mathbf{M}_c = [0 \ 0 \ M_{cz}]^T$, $\mathbf{F}_c = [F_{cx} \ F_{cy} \ 0]^T$, and $\mathbf{f} = [f_x \ f_y \ 0]^T$. Fig. 3 shows a schematic of interaction forces on the needle carrier system. The elements of the distributed interaction force vector \mathbf{f} can be obtained using Fig. 3 as

$$f_x = f_{cx} + f_{fx} \quad (9a)$$

$$f_y = f_{cy} + f_s + f_k + f_{fy} \quad (9b)$$

where

$$\begin{aligned} f_s(x) &= F_s H_{l-X}(x), & f_k(x) &= K_t \omega [H_{x_t}(x) - H_{x_t+l_t}(x)] \\ f_{cx}(x) &= -F_{c\xi} - F_{c\eta} \omega'(l, t), & f_{cy}(x) &= [F_{c\eta} - F_{c\xi} \omega'(l, t)] \delta_\ell(x) \\ f_{fx}(x) &= F_f H_{l-X}(x), & f_{fy}(x) &= F_f \omega' H_{l-X}(x) \end{aligned} \quad (10)$$

where $x_t = l - X - d_t - l_t$. In (10), we have used assumption 3 and assumed $\tan(\omega') = \omega'$. The transverse and axial component of F_c in (10) can be related by the bevel angle using $F_{c\xi} = F_{c\eta} \tan(\alpha)$ (see Fig. 3).

We note that some of the above mentioned forces are moving loads acting over a specific length of the needle. As the needle is inserted, their point of application or width will change accordingly. To define the limits of the force

profile applied to the length of the beam, we use unit step (H) and Dirac delta (δ) functions. The shorthand notation $H_{x_0}(x) = H(x - x_0)$ and $\delta_{x_0}(x) = \delta(x - x_0)$ describes unit step and Dirac delta functions shifted by the constant x_0 .

Note that in (10) we have used (4b) to transform the contact forces shown in Fig. 3 from their point of application to the body-fixed frame. Consequently, all the forces given in (9) are in terms of the body-fixed frame (xy).

Having all the reaction forces defined, we can continue to derive the virtual work (\mathcal{W}). Using (1), we can express the virtual displacement $\delta \mathbf{R}_N$ in the body fixed-frame as $\delta \mathbf{R}_N = C \delta \mathbf{R} + (\tilde{\mathbf{u}}^T + \tilde{\mathbf{r}}^T) \delta \theta + \delta \mathbf{u}$. Plugging $\delta \mathbf{R}_N$ into (8) gives

$$\begin{aligned} \bar{\delta} \mathcal{W} = & \delta \theta^T \mathbf{M}_c + \delta \mathbf{R}^T \mathbf{C}^T \mathbf{F}_c \\ & + \int_0^l [\delta \mathbf{R}^T \mathbf{C}^T \mathbf{f} + \delta \theta^T (\tilde{\mathbf{u}} + \tilde{\mathbf{r}}) \mathbf{f} + \delta \mathbf{u}^T \mathbf{f}] dx \end{aligned} \quad (11)$$

Combining (6), (7), and (11) and considering the geometrical constraints (4a) and (4b), we can write the Lagrangian in general functional form as

$$\mathcal{L} = \mathcal{L}(\mathbf{u}, \dot{\mathbf{u}}, \mathbf{u}', \mathbf{u}'', \mathbf{R}, \mathbf{V}, \boldsymbol{\theta}, \dot{\boldsymbol{\theta}}) \quad (12)$$

Inserting the Lagrangian in the extended Hamilton's principle given by (5) and following the mathematical procedure first introduced in [19], we can obtain

$$\begin{aligned} & \int_{t_1}^{t_2} \delta \mathbf{R}^T \left[\mathbf{C}^T \left(-\frac{d}{dt} \left(\frac{\partial \mathcal{L}}{\partial \mathbf{V}} \right) - \tilde{\boldsymbol{\theta}} \frac{\partial \mathcal{L}}{\partial \boldsymbol{\theta}} + \mathbf{F}_c + \int_o^l \mathbf{f} dx \right) + \frac{\partial \mathcal{L}}{\partial \mathbf{R}} \right] dt \\ & + \int_{t_1}^{t_2} \delta \boldsymbol{\theta}^T \left[-\frac{d}{dt} \left(\frac{\partial \mathcal{L}}{\partial \boldsymbol{\theta}} \right) - \tilde{\mathbf{V}} \frac{\partial \mathcal{L}}{\partial \boldsymbol{\theta}} + \frac{\partial \mathcal{L}}{\partial \boldsymbol{\theta}} + \mathbf{M}_c + \int_o^l (\tilde{\mathbf{u}} + \tilde{\mathbf{r}}) \mathbf{f} dx \right] dt \\ & + \int_{t_1}^{t_2} \int_o^l \delta \mathbf{u}^T \left[\frac{\partial \hat{\mathcal{L}}}{\partial \mathbf{u}} - \frac{d}{dt} \left(\frac{\partial \hat{\mathcal{L}}}{\partial \dot{\mathbf{u}}} \right) - \frac{d}{dx} \left(\frac{\partial \hat{\mathcal{L}}}{\partial \mathbf{u}'} \right) + \frac{d^2}{dx^2} \left(\frac{\partial \hat{\mathcal{L}}}{\partial \mathbf{u}''} \right) + \mathbf{f} \right] dx dt \\ & + \int_{t_1}^{t_2} \left[\delta \mathbf{u}'^T \frac{\partial \hat{\mathcal{L}}}{\partial \mathbf{u}''} + \delta \mathbf{u}^T \left(\frac{\partial \hat{\mathcal{L}}}{\partial \mathbf{u}'} - \frac{d}{dx} \left(\frac{\partial \hat{\mathcal{L}}}{\partial \mathbf{u}''} \right) \right) \right] \Big|_0^l dt = 0 \end{aligned} \quad (13)$$

At this point we simplify the integrals in (13) to derive the hybrid equations for the needle-carrier system. The fundamental lemma of the calculus of variations tells us that the integrands in the four integrals in (13) must vanish. The first two integrals in (13) will give us the Lagrangian equations for the carrier. Following the mathematical approach presented in [19] we obtain the dynamic equations of the system.

We restrict the motion of the carrier to a linear insertion along the X direction (see Fig. 1). However, using (13) we calculate all the force/torque applied to the carrier. From the first two integrals in (13) we obtain the dynamic equations of the rigid part in terms of quasi-coordinates

$$F_{cx} = m_c \ddot{X} - \int_0^l f_x dx \quad (14a)$$

$$F_{cy} = m_c g + \rho A \int_o^l \ddot{\omega} dx - \int_0^l f_y dx \quad (14b)$$

$$M_{cz} = \int_0^l \left\{ -\rho A \left[\dot{\omega} \dot{X} + \omega \ddot{X} + \ddot{\omega} (u + x) \right] - \omega f_x + (x + u) f_y \right\} dx \quad (14c)$$

where f_x and f_y are given by (9) and (10). Note that based on Assumption 2, we can say that u , the needle shortening along the x direction of the body-fixed frame, is small. Thus, we have neglected the term \ddot{u} in derivation of (14).

Next, we will derive the equation of motion for the continuous part of the system. Inserting the forces given by (9) and (10) in the last two integrals in (13), taking integration by

parts, and performing simple mathematical operations when appropriate, we obtain the PDE governing the motion of the needle as

$$EI\omega''' + \rho A\ddot{\omega} + P\omega'' = Q \quad (15)$$

with P and Q being

$$Q = f_s + f_k + F_{cn}\delta_\ell(x) - F_{cn}\omega'^2\delta_\ell(x) \quad (16a)$$

$$P = F_{c\xi} + F_f(\ell - x)H_{\ell-X} + F_{cn}\omega'(\ell, t) \quad (16b)$$

subject to the following set of boundary conditions:

$$\omega(0, t) = 0, \quad \omega'(0, t) = 0, \quad \omega''(\ell, t) = 0, \quad \omega'''(\ell, t) = 0 \quad (17)$$

Equations (14) and (15) represent a set of coupled ordinary and partial differential equations describing the motion of the needle-carrier system. The partial differential equation (PDE) in (15) implies that the dimensionality of the problem is infinite. Also, the hybrid equations are nonlinear and complicated to solve. In the next step, we will simplify the equations by discretizing the continuous part and reducing the size of the model.

C. Discretization of the Continuous PDE

In this section, the continuous model in (15) is replaced by a discrete model following an approach known as Bubnov-Galerkin method [20]. This approach has been previously used to simplify nonlinear PDEs [12]. The displacement field is approximated using $\omega(x, t) \approx \hat{\omega}(x, t) = \sum_{i=1}^n \phi_i(t)W_i(x)$, where $W_i(x)$ ($i=1, \dots, n$) is assumed function representing the first n modes of vibration and $\phi_i(t)$ ($i=1, \dots, n$) are the generalized coordinates or time functions expressing the deformation of the beam with respect to time. We select the mode shapes of a homogeneous clamped-free beam as the assumed functions. This way we ensure that the assumed functions satisfy the differentiation requirements and geometrical and dynamic boundary conditions in (17). The mode shapes for the clamped-free beam are given by [21]

$$W_i(x) = \frac{1}{\kappa_i} \left[-\gamma_i \left(\cos\left(\frac{\beta_i x}{\ell}\right) - \cosh\left(\frac{\beta_i x}{\ell}\right) \right) + \sin\left(\frac{\beta_i x}{\ell}\right) - \sinh\left(\frac{\beta_i x}{\ell}\right) \right] \quad (18)$$

where β_i ($i=1, \dots, n$) is a dimensionless constant corresponding to different modes of vibration. In this work, we will estimate the continuous model given in (15) using the first four modes. Values of the first four β_i for a clamped-free beam are 1.857, 4.694, 7.855 and 10.996, respectively [21]. γ and κ in (18) are given by

$$\gamma_i = \frac{\sin\beta_i + \sinh\beta_i}{\cos\beta_i + \cosh\beta_i}, \quad \kappa_i = -\gamma_i(\cos\beta_i - \cosh\beta_i) + \sin\beta_i - \sinh\beta_i \quad (19)$$

Following the Bubnov-Galerkin method and inserting the approximated displacement field in (15) we can get a finite-dimensional reference model of needle steering as

$$\hat{\mathbf{M}}\ddot{\boldsymbol{\phi}} + \hat{\mathbf{K}}\boldsymbol{\phi} + \hat{\mathbf{R}}\boldsymbol{\phi} + \hat{\mathbf{T}}\boldsymbol{\phi} + \hat{\mathbf{G}}\boldsymbol{\phi}\boldsymbol{\phi}^T \mathbf{W}'(\ell) = \hat{\mathbf{S}}(\boldsymbol{\phi}) + \hat{\mathbf{V}} \quad (20)$$

where elements of matrices and vectors in (20) are given by

$$\begin{aligned} \hat{M}_{ij} &= \rho A \int_0^\ell W_j(x)W_i(x)dx, & \hat{K}_{ij} &= EI \int_0^\ell W_j'''(x)W_i(x)dx, \\ \hat{R}_{ij} &= F_f \int_{\ell-X}^\ell (\ell-x)W_j''(x)W_i(x)dx + F_{c\xi} \int_0^\ell W_j''(x)W_i(x)dx, \\ \hat{T}_{ij} &= -K_t \int_{x_t}^{x_t+l_t} W_j(x)W_i(x)dx, & \hat{S}_i &= \int_{\ell-X}^\ell F_s(x, t)W_i(x)dx, \\ \hat{G}_{ij} &= F_{cn} \left[W_j'(\ell) + \int_0^\ell W_j''(x)W_i(x)dx \right], & \hat{V}_i &= F_{cn} \end{aligned} \quad (21)$$

By solving the above system of ODEs, the time functions $\phi_i(t)$ and consequently the needle deflection can be found. The matrices $\hat{\mathbf{M}}$ and $\hat{\mathbf{K}}$ are constant and time invariant and correspond to the kinetic energy of the system and the elastic linear forces in the beam, respectively. As we use orthogonal eigenfunctions of a homogeneous clamped-free beam as the assumed modes, $\hat{\mathbf{M}}$ and $\hat{\mathbf{K}}$ are both positive definite and symmetric. $\hat{\mathbf{T}}$ corresponds to the effects of reaction forces from the template. $\hat{\mathbf{R}}$ contains the effects of non-conservative axial forces, i.e., friction and axial component of the cutting force. The last term on the right side of the system of differential equations in (20) is due to the rotation of needle tip as it bends under external forces. $\hat{\mathbf{S}}$ shows the effects of tissue reaction force. Sign of elements of $\hat{\mathbf{S}}$ can change during the needle insertion based on the shape and orientation of the needle. $\hat{\mathbf{V}}$ corresponds to the transverse component of the cutting force acting at the tip of the needle. After 180° needle rotation, orientation of cutting force and consequently sign of $\hat{\mathbf{V}}$ will change.

So far, we have modelled the dynamics of the coupled needle-carrier system. However, the interaction forces shown in Fig. 3, including the tissue reaction force (F_s) and the cutting force (F_c) are yet to be determined. In the next section we will model the needle/tissue interaction forces.

III. MODELING: NEEDLE/TISSUE INTERACTION FORCES

Fig. 3 shows a schematic of the interaction forces applied to the needle during needle insertion. The needle interactions with surrounding environment are modelled by axial and transverse distributed and concentrated loads that are applied to the portion of the needle that is inside the tissue. During needle insertion, the cutting force F_c is applied to the needle in a direction perpendicular to the beveled tip. The transverse and axial component of F_c are related using $F_{c\xi} = F_{cn}\tan(\alpha)$ (see Fig. 3). A force distribution F_s is used to model tissue reaction forces as the result of its deformation caused by needle bending. The grid template acts as a rigid support and is modelled by a stiff spring with stiffness of K_t . It is positioned at distance d_t from the tissue and has length l_t . Friction between the needle shaft and the tissue is modelled by an axially distributed load F_f tangent to the needle shaft.

In order to model the friction force F_f , will use the the LuGre model, which has been previously used to calculate needle-tissue friction force along the needle shaft during needle steering [22]. For brevity, details of the friction force model is not considered in the analyses that follow. A complete description of friction force model can be found in [22]. In the following, we will model the remaining components of the needle/tissue interaction force including the tissue cutting force F_c and tissue reaction force F_s .

A. Cutting Force

In needle insertion, cutting through tissue results in a relatively large cutting force at the needle tip [23]. Modeling soft tissue cutting for robotic needle steering and surgical planning has been the topic of significant research efforts [24], [25]. In most previous studies cutting force is assumed to be constant [12], [23]. However, experimental studies show that cutting force depends on insertion velocity and changes during the insertion [25]. Here, we propose a method based on principles of fracture mechanics in elastic materials to relate

cutting force to velocity-dependent tissue fracture toughness. It is a valid assumption to model the tissue around the needle tip as pure elastic, as when cutting happens relatively fast, there is no delayed viscoelastic crack growth, and the near tip plastic zone is small [26]. Fracture toughness, G_c , is a material property and a measure of resistance against crack growth in linear elastic materials. Based on the definition of fracture toughness, crack extension occurs when the rate of energy release in crack extension, G , is equal or greater than G_c . Under plain strain condition, fracture toughness is

$$G_c = \frac{K_I^2}{E'} \quad (22)$$

where $E' = \frac{E}{1-\nu^2}$. K_I is the stress intensity factor for mode I fracture. Mode I or opening mode corresponds to fracture in a body loaded by tensile forces such that the crack surfaces move apart in the direction of applied forces. Microscopic observations of tissue cutting have shown mode I crack best represents crack geometry during tissue cutting [2]. (22) corresponds to quasi-static cutting. In dynamic fracture, the crack driving force should incorporate the effects of kinetic energy and crack velocity. It has been shown that the dynamic energy release rate in elastic material can be expressed as [26]

$$G(t) = \mathcal{A}(V) \frac{K_{ID}^2(V)}{E'} \quad (23)$$

Two approximate expressions for $\mathcal{A}(V)$ and $K_{ID}(V)$ are [26]

$$\mathcal{A} = \left[(1 - hV) \left(1 - \frac{V}{c_r} \right) \right]^{-1}, \quad K_{ID} = \frac{K_{I0}}{1 - \left(\frac{V}{V_l} \right)^m} \quad (24)$$

where h is a function of shear and longitudinal wave speeds and constant for a given material and m is an experimentally determined constant. Clinical needle insertion velocities vary in between 5 to 50 mm/sec [27], which is significantly smaller than the Raleigh surface wave speed in soft tissue [28]. Also, h is zero for homogeneous isotropic materials and negligible at low crack velocities for non-homogeneous materials [26]. Thus, we can assume \mathcal{A} is equal to one.

(23) and (24) state that the dynamic stress intensity factor and consequently fracture toughness are functions of insertion velocity in the dynamic crack propagation, and that material resistance increases with crack speed. Based on (24), at low insertion speeds, K_{ID} is relatively insensitive to V but K_{ID} increases asymptotically as V reaches the limiting value of V_l . Now, we can use the equation proposed in [25] to relate cutting force to fracture toughness

$$F_c = G(t) w_c \quad (25)$$

w_c is the cutting width and equal to the needle outer diameter.

B. Tissue Reaction Force

The 2D distributed force F_s shown in Fig. 3 represents needle-tissue interaction forces due to tissue compression. In order to find F_s , first we calculate the tissue deformation as a result of needle deflection. Next, we implement a viscoelastic tissue model to relate the tissue reaction force to the the tissue deformation and obtain F_s .

The magnitude of the approximated interaction forces are relative to the total deformation of tissue caused by needle deflection. However, since the needle cuts a path through the tissue as it is inserted, the tissue deformation is not exactly equal to the needle transverse deflection. This can be understood more easily if we discretize an infinitesimal insertion of

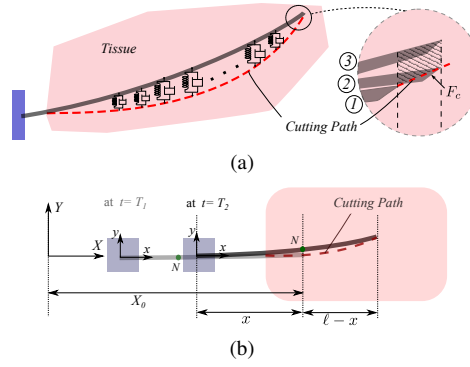


Fig. 4. A schematic of needle insertion in soft tissue. (a) Infinitesimal tissue cutting consists of three steps: 1) needle at the beginning of insertion; 2) needle cutting through the tissue; 3) cutting force applied perpendicularly to the tip causing needle deflection and tissue deformation. Tissue deformation is the difference between the cutting path and the final needle position (hatched area) and less than the needle deflection from its unbent position. Tissue reaction force is modelled by series of Kelvin-Voigt viscoelastic elements placed in between the cutting path and the needle. (b) Schematic of needle insertion and cutting path at times T_1 and T_2 .

the needle into three parts, namely, pre-cutting, tissue cutting, and tissue deformation (see Fig. 4(a)). In the cutting phase, the needle cuts through the tissue and opens up a path called *cutting path*. Then, cutting force is applied perpendicularly to the tip and causes needle deflection. Consequently, the soft tissue is deformed by as much as the difference between the cutting path and the final needle position.

To find the tissue reaction forces applied to a certain element of the needle, we calculate the amount of tissue deformation by comparing the global deflection of the needle element (i.e., needle shape) with the global position of needle tip (i.e., the cutting path) when it was in the current position of the needle element. This fact is explained in Fig. 4(b). We are interested in finding the tissue deformation in the proximity of the point N on the needle, which is located at position X_0 with respect to the inertial frame at the present time ($t=T_2$). To this end, we need to find the needle cutting path and compare it to the current needle deflection. The cutting path is the needle tip deflection when it passed X_0 at a time $t=T_1 < T_2$. This has to be compared to the current deflection of the needle (position of point N) at $t=T_2$. The difference is the tissue deformation at position X_0 with respect to the inertial frame at the present time ($t=T_2$).

Based on Fig. 4(b), the tissue deformation is equal to $\omega(x, t) - \omega(\ell, t - \tau)$, where τ is the time delay used to find the cutting path at the current position of point N on the needle, and $\omega(\ell, t - \tau)$ is the deflection of the needle tip or the cutting path at time $t - \tau$. In Fig. 4(b), for element N of the needle, we have $\tau = T_2 - T_1$. Also, Assuming needle deflection is relatively small compared to the length of the needle, using Fig. 4(b) we can say $\tau = \frac{\ell - x}{V}$, where V is the needle insertion velocity.

Now to relate tissue deformation to tissue reaction force, we use a conventional viscoelastic model known as the Kelvin-Voigt model. In Kelvin-Voigt model, tissue is modelled as a Hookean spring in parallel with a Newtonian damper. The tissue reaction force can be defined as

$$F_s(x, t) = K_s [\omega(x, t) - \omega(\ell, t - \tau)] + C_s \dot{\omega}(x) \quad (26)$$

The presented novel tissue interaction model enables accounting for the effect of 180° axial rotation of the needle tip on the needle deflection. When the needle is axially rotated

during the insertion, the orientation of the bevel tip changes and consequently the direction of the transverse component of cutting force changes too, causing the needle to bend in the opposite direction. The part of the needle that is already inside the tissue is forced to stay close to the path produced by the needle beforehand, i.e., the cutting path. Thus, the needle is confined in the tissue and the model can simulate multiple bending in the needle as a result of axial needle rotations.

The tissue reaction force model given by (26) is in fact a time-delayed system. F_s , the tissue reaction force is a function of the needle deflection at previous times. Control of time-delayed systems is very challenging and, therefore, it is desirable to simplify the system. Here, a novel mathematical approach is presented to reduce the time-delayed system of differential equations to a simple system of ODEs. In our approach we use previous values of the system states to estimate the current ones. This idea was first proposed in [29].

Introducing (26) into \hat{S} in (21) and substituting assumed-mode approximation for the needle deflection gives

$$\begin{aligned} \hat{S}_i = & \int_{\ell-X}^{\ell} \left[K_s \sum_{m=1}^n \phi_m(t) W_m(x) + C_s \sum_{k=1}^n \dot{\phi}_k(t) W_k(x) \right] W_i(x) dx \\ & - \int_{\ell-X}^{\ell} \left[K_s \sum_{j=1}^n \phi_j(t-\tau) \right] W_i(x) dx \end{aligned} \quad (27)$$

The second integral in (27) contains the delay term, τ . Now by expanding the delay term in (27) and replacing x as a function of the delay by $\tau = \frac{\ell-x}{V}$ gives

$$\begin{aligned} & \int_{\ell-X}^{\ell} \left[K_s \sum_{j=1}^n \phi_j(t-\tau) \right] W_i(x) dx \\ & = \frac{K_s V}{\kappa_i} \int_0^t \left[\sum_{j=1}^n \phi_j(t-\tau) \left(\sin(\lambda_i \tau + \beta_i) - \gamma_i \cos(\lambda_i \tau + \beta_i) \right) \right] d\tau \\ & + \frac{K_s V}{\kappa_i} \int_0^t \left[\sum_{k=1}^n \phi_k(t-\tau) \left(-\sinh(\lambda_i \tau + \beta_i) + \gamma_i \cosh(\lambda_i \tau + \beta_i) \right) \right] d\tau \end{aligned} \quad (28)$$

where $\lambda_i = \frac{-\beta_i V}{\ell}$. Close scrutiny of (28) reveals that the above technique has transformed the system of ODEs in (27) to a convolution integral. This is very promising because it facilitates solving (27) without having to deal with the system delay. Below, we tackle the problem by determining an equivalent system whose time response will take the form of the convolution integral in (28), i.e., the same as the time response of the ODE system in (27).

To do so, first we take Laplace transform of the two terms on the right side of (28), next we sort out the equations and perform basic mathematical simplifications. Finally, taking inverse Laplace gives

$$\begin{aligned} \ddot{\varphi}_{ij} + \lambda_i^2 \varphi_{ij} &= [\sin(\beta_i) - \gamma_i \cos(\beta_i)] \dot{\phi}_j + \lambda_i [\gamma_i \sin(\beta_i) + \cos(\beta_i)] \phi_j \\ \ddot{\chi}_{ij} - \lambda_i^2 \chi_{ij} &= [-\sinh(\beta_i) + \gamma_i \cosh(\beta_i)] \dot{\phi}_j + \lambda_i [\gamma_i \sinh(\beta_i) - \cosh(\beta_i)] \phi_j \end{aligned}$$

With two new state variables

$$\begin{aligned} \varphi_{ij}(t) &= \int_0^t \phi_j(t-\tau) \left(\sin(\lambda_i \tau + \beta_i) - \gamma_i \cos(\lambda_i \tau + \beta_i) \right) d\tau, \\ \chi_{ij}(t) &= \int_0^t \phi_j(t-\tau) \left(-\sinh(\lambda_i \tau + \beta_i) + \gamma_i \cosh(\lambda_i \tau + \beta_i) \right) d\tau \end{aligned} \quad (29)$$

Using the new state variables, we can eliminate the delay in the needle steering model and rewrite the term corresponding to the tissue model (\hat{S}) in (21) as

$$\hat{D}\dot{\phi} + \hat{N}\phi + \varsigma = 0 \quad (30)$$

where

$$\begin{aligned} \hat{D}_{ij} &= C_s \int_{\ell-X}^{\ell} W_j(x) W_i(x) dx, \quad \hat{N}_{ij} = K_s \int_{\ell-X}^{\ell} W_j(x) W_i(x) dx, \\ \varsigma_i &= -\frac{K_s V}{\kappa_i} \sum_{j=1}^n (\varphi_{ij}(t) + \chi_{ij}(t)) \end{aligned} \quad (31)$$

Note that (30) is the needle-tissue interaction model and depends only on the needle shape and the tissue mechanical characteristics and we have eliminated the delay term. The main assumption of the proposed approach is that the continuous states and system dynamics remain almost unchanged during sampling time which is valid for control and simulation of needle insertion at high sampling frequencies. (30) is a system of ODEs that should be solved in conjunction with the needle steering model in (20) to find the needle deflection.

IV. EXPERIMENTAL MODEL IDENTIFICATION AND VALIDATION

A. Materials and Equipment

In order to perform needle insertion into soft tissue, the setup shown in Fig. 5(a) is used. Two different needles are used to perform insertions. One is a standard 18-gauge brachytherapy needle (Eckert & Ziegler BEBIG Inc., CT, USA) made of stainless steel. The second needle is more flexible and made of Nitinol wire (Kellogg's Research Labs, Plymouth, NH, USA) with a diameter of 1 mm and a length of 18 mm. The wire is inserted into the tip of a shortened needle with length of 1.2 mm and fixed in place with adhesive. The values of the needles physical parameters are given in Table II. In order to evaluate the ability of the model in capturing the effects of the grid template on needle deflection, an 18G grid template is used in certain needle insertions.

Three different tissue samples are used in the experiments: plastisol, porcine gelatin, and ex-vivo beef. The plastisol tissue is made of 80% (by volume) liquid plastic and 20% plastic softener (M-F Manufacturing Co., USA). The gelatin phantom is made by mixing porcine gelatin powder (Sigma-Aldrich Co., Canada) with water at a temperature of 70°C. The weight ratio of gelatin-to-water in the mixture is 18%. For ex-vivo tests, a piece of beef loin is used. Bovine tissue is embedded in gelatin to get a smoother surface on top, thus increasing the contact surface between the ultrasound probe and the tissue and as a result reducing noise in the ultrasound images. Young's elasticity moduli of the three tissues calculated using indentation tests, are reported in Table I. The elasticity of the synthetic tissues are similar to what is found in animal tissue [30].

B. Characterization of Needle-Tissue Interaction Forces

Experiments are designed and performed to identify the parameters of the friction, cutting force, and soft tissue models. To identify the parameters of the friction force model, friction forces along needle shaft must be accurately measured. To do so, similar experiment as what is presented in [24] is used to separately measure the friction force by eliminating

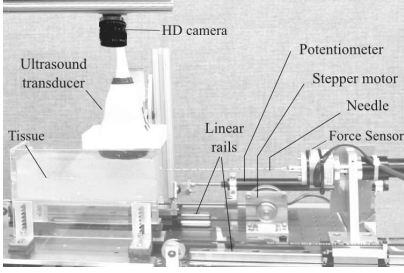


Fig. 5. Experimental setup used to perform needle insertion experiments. The setup consists of a robotic system with two DoFs, namely the translational and rotational motions of needle. Forces and torques are measured at the needle base using a 6-DOF force/torque sensor (ATI Nano 43, ATI Industrial Automation, USA). Images for needle tip and shape tracking inside transparent phantom tissues are recorded using an HD Sony camera (XCL-S800, Sony of Canada Ltd., Canada) and an Ultrasound machine (SonixTouch, Ultrasonix, Canada) is used to track needle tip position in ex-vivo tissue.

TABLE I
EXPERIMENTALLY IDENTIFIED MODEL PARAMETERS.

Models → Cases (Tissues) ↓	Cutting force model			Soft tissue model				
	V_t [m/sec]	K_{t0} [Pa \sqrt{m}]	m	$RMSE$ [N]	E [kPa]	K_s [N/m ²]	C_s [N.sec/m ²]	$RMSE$ [mm]
Gelatin	0.145	2.707e6	1.117	0.079	59.9	1.583e5	8.569e3	0.197
Plastisol	0.177	7.620e5	0.851	0.087	25.6	0.598e5	8.010e4	0.408
Bovine Tissue	0.280	1.134e6	0.838	0.081	24.5	3.202e5	9.618e4	0.251

or minimizing the influence of other interaction forces such as cutting force and the tissue compression force. To identify the friction model parameters, we employed the procedure based on friction-velocity mapping introduced in [31]. Friction-velocity mapping was developed by inserting the needle using a sinusoidal signal with an initial frequency of 0.05 Hz, reaching to 0.2 Hz in 250 seconds. Four trials are performed for each combination of tissue and needle at four different insertion points.

To measure the magnitude of the cutting force, a shortened needle is inserted into the tissue at 30 different constant velocities between 5 and 40 mm/sec. Knowing the magnitude of friction from the model identified in the previous step, we can simply calculate the magnitude of the cutting force for different insertion velocities. Using measured values, the parameters of the fracture-based cutting force model presented by (23) and (24) are identified. Fig. 6(a) displays the mean cutting force over the trials versus needle insertion velocity. As predicted by (23) and (24), the average cutting force is an increasing function of velocity. The values of identified parameters are presented in Table I. Root-mean-square error (RMSE) is calculated as $\sqrt{\frac{\sum_{k=1}^n (\hat{y}_k - y_k)^2}{n}}$ and is used as a measure of the differences between values predicted by each identified model, \hat{y} , and the values actually observed in the experiments, y , for n data points.

The purpose of the next experiment is to identify the parameters of the viscoelastic model of the tissue (i.e., K_s and C_s). First, a relaxation test is performed to estimate the values of K_s and C_s . Next, in order to calculate the values of K_s and C_s in (26) more precisely, we fitted the deflection data for three insertions at three different velocities (10, 20, and 50 mm/sec) to the proposed model of needle steering given in (20) and (30) by performing a multi-objective optimization.

The relaxation test is performed by giving a position step input to the indenter and measuring the exerted force. The experiments are performed with an insertion velocity of 10 mm/sec and indentation depths of 5, 8, 10 mm. Knowing tissue stiffness (Young modulus) from previous indentation tests, we

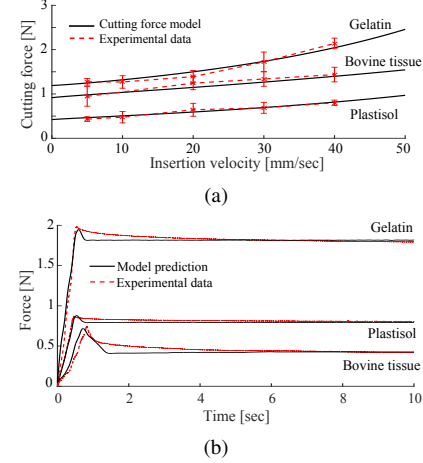


Fig. 6. (a) A comparison between experimentally-obtained cutting force and cutting force model prediction versus insertion velocity. Error bars denote standard deviation. (b) Experimental and tissue model prediction results for relaxation test with input displacement of 8 mm at insertion velocity of 10 mm/sec.

TABLE II
VALUES OF CONSTANT KNOWN PARAMETERS OF THE MODEL.

Brachytherapy needle							
E [GPa]	ℓ [m]	ρ [kg/m ³]	r_{in} [m]	r_{out} [m]	A [m ²]	I [m ⁴]	α [°]
200	0.2	8030	0.5e-3	0.63e-3	4.81e-7	7.75e-14	20
Nitinol wire							
E [GPa]	ℓ [m]	ρ [kg/m ³]	r_{out} [m]	A [m ²]	I [m ⁴]	α [°]	
75	0.18	6500	0.5e-3	7.85e-7	1.962e-13	20	
Grid template							
K_t [N/m]	l_t [m]		d_t [m]		m_c [kg]		
10e7	0.02		0.005		0.045		

can calculate tissue viscosity by fitting the data to the Kelvin-Voigt model using the least-squares method. For relaxation tests for 8 mm indentations, tissue model predictions are shown in Fig. 6(b). Later, values of the identified parameters from the tissue relaxation tests are used to define the initial values and lower and upper boundaries in the optimization algorithm. Genetic algorithm is used to perform multi-objective optimization and minimize the residual error between the experimental data points and the predicted ones with the goal of finding values of K_s and C_s [32]. Table I provides the final values of the identified parameters and RMSE of the fitted models.

C. Model Validation Results and Discussion

In validation experiments, the insertion depth is fixed for each needle type – 140 mm for the brachytherapy needle and 120 mm for the Nitinol wire. The needle shape and tip deflection are computed through image processing. For the gelatin and plastisol tissues, images are acquired using the HD camera (see Fig. 5(a)). For insertions in the bovine tissue, ultrasound images are used to find the needle deflection using the method proposed in [33]. The values of the known model parameters used in simulations are given in Table II. These include the needle-carrier system properties and the needle geometric parameters. The stiffness of the spring modeling the template is arbitrarily chosen to be very large (10e7 N/m).

Fig. 7 shows the needle deflection for the different needles inserted through various soft tissues at velocities of 5, 20, and 40 mm/sec. The magnitude of needle deflection is close to the reported clinically obtained data in brachytherapy [34]. Table III compares the experimental and model prediction of tip deflection values at 6 different velocities for insertion, each of which has been attempted 5 times. Final tip position in the experiments $\omega_{exp}(\ell)$, final tip position in the simulation

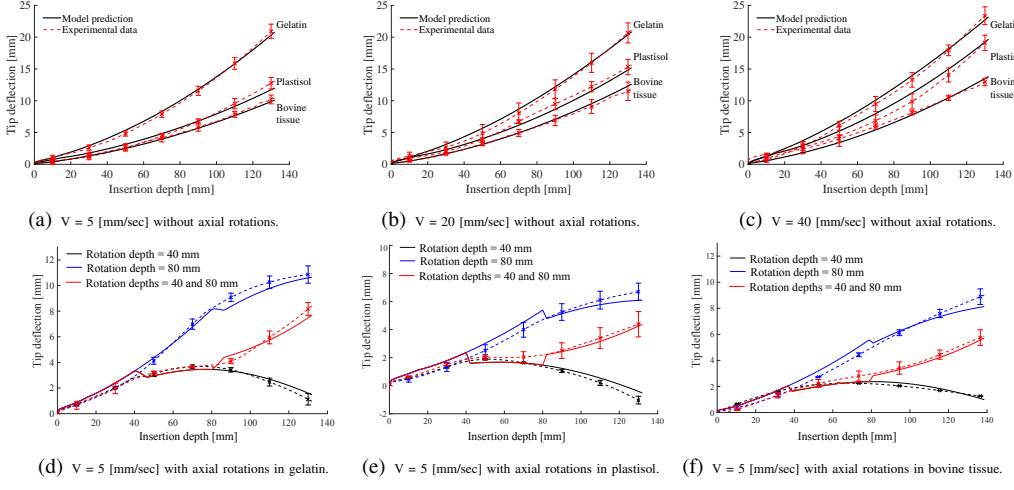


Fig. 7. A comparison of experimentally-obtained needle tip deflections and the corresponding model predictions for needle insertion in plastisol, gelatin, and bovine tissue. (a) $V=5$ [mm/sec] without axial rotations. (b) $V=20$ [mm/sec] without axial rotations. (c) $V=40$ [mm/sec] without axial rotations. (d) $V=5$ [mm/sec] with axial rotations in gelatin. (e) $V=5$ [mm/sec] with axial rotations in plastisol. (f) $V=5$ [mm/sec] with axial rotations in bovine tissue. Solid and dashed lines denote model prediction and experimental data, respectively.

$\omega_{sim}(\ell)$, maximum tip error e_{max} , and standard deviation of final tip position $\sigma(\ell)$ are listed in Table III. The largest deviation in final tip deflection was observed for plastisol at insertion velocity of 50 mm/sec (7%), while the smallest difference was observed for gelatin at insertion velocity of 5 mm/sec (3.2%).

The maximum and minimum prediction errors of the model in [12] for needle insertion in plastisol-based tissue is 6% and 3% for insertion velocities of 5 and 40 mm/sec, respectively. Compared to our previous model [12], the proposed model shows a similar fit to experimental data for different insertion velocities. However, the model presented in [12] is not capable of modeling needle deflection with axial rotation(s).

We also performed some experiments involving 180° axial rotation of the needle. The brachytherapy needle is inserted to a total depth of 140 mm in the soft tissues at a speed of 5 mm/s while either a single rotation is performed at a depth of 40 or 80 mm, or double rotations are performed at depths of 40 and 80 mm. Four needle insertions are performed for each scenario. A well-tuned PID controller was used to rotate the needle tip in less than 0.2 sec as it was inserted, thus ensuring the needle stayed in the insertion plane. The resulting needle tip deflection is shown in Fig. 7. The results of this experiment are summarized in Table III. The model captures the effect of axial tip rotation on the needle deflection for all three tissues and the maximum error in predicting the tip position is 0.74 mm at a depth of 135 mm for insertion in gelatin with a double rotation. In model predictions, when the needle is axially rotated, there is a small jump in needle trajectory that corresponds to a sudden change of the cutting force orientation. However, this sudden deflection is small (a maximum of 0.61 mm in plastisol) and has almost no effect on the needle tip trajectory predictions. The magnitude of this jump depends on the value of the cutting force, insertion velocity, depth of rotation and tissue characteristics.

Fig. 8 shows results of needle insertions performed with the template for the plastisol tissue at velocities of 5, 20 and 40 mm/sec. Five insertions were performed for each velocity. As expected, the template decreases the total needle deflection by restraining the needle motion outside the tissue.

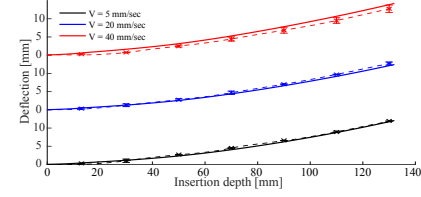


Fig. 8. Experimental needle tip deflection and model prediction for needle insertion in plastisol with the grid template. Solid and dashed lines denote model prediction and experimental data, respectively.

Also, the template reduces the effect of insertion velocity on the needle tip deflection – the difference between the final tip deflections at velocities of 5 and 50 mm/sec is less than 4 mm. Results show the model can perfectly explain the template effect on needle deflection with maximum final tip error of 0.72 mm for insertion velocity of 40 mm/sec.

We also performed insertions using the more flexible needle made of Nitinol wire. Fig. 9 presents the results of experimental needle insertions in synthetic tissues compared to model simulation results. Needle was inserted at a velocity of 5 mm/sec with and without rotation(s). Four needle insertions were performed for each scenario. In all of the experiments with the wire, the template was used. The prescribed needle insertion depth for wire was 120 mm. Fig. 9 indicates that the model is in good agreement with the experimental results. The maximum error in predicting the tip deflection is 1.1 mm at a depth of 121 mm for insertion in plastisol. Also, the maximum error of the model in predicting the final tip position is 0.432 mm for insertions with double rotation in plastisol.

As mentioned before, one of the advantages of the proposed hybrid formulation of needle steering is that we can explicitly see the effect of the needle base force/torque on needle deflection and vice versa. To validate the model in terms of the dynamics of the carrier, we compare the force/torque applied to the carrier (i.e., the needle driving robot in our experiments) with the needle base force/torque measured during needle insertions in plastisol tissue. Fig. 10 shows a comparison of experimentally-obtained axial and lateral forces and in-plane torque applied to the needle's base during needle insertion in plastisol for three different trials and the model predictions of

TABLE III
RESULTS OF INSERTION OF THE NEEDLE AT DIFFERENT VELOCITIES WITH AND WITHOUT AXIAL ROTATION(S).

V [mm/sec]	Rotation depth(s)	Gelatin			Plastisol			Bovine tissue								
		$\omega_{exp}(\ell)$ [mm]	$\omega_{sim}(\ell)$ [mm]	e_{max} [mm]	$\sigma(\ell)$ [mm]	RMSE [mm]	$\omega_{exp}(\ell)$ [mm]	$\omega_{sim}(\ell)$ [mm]	e_{max} [mm]	$\sigma(\ell)$ [mm]	RMSE [mm]					
5	-	21.47	20.80	0.67	1.11	0.348	13.09	12.20	0.88	0.91	0.576	10.44	10.11	0.47	0.68	0.189
10	-	22.04	21.11	0.93	0.94	0.421	13.85	13.48	0.49	0.56	0.442	10.25	11.16	0.91	0.43	0.373
20	-	21.14	20.85	0.49	1.50	0.466	15.62	15.39	0.63	1.01	0.423	11.85	12.61	0.72	1.14	0.278
30	-	22.51	22.14	0.82	1.32	0.507	16.95	18.36	1.41	1.15	0.621	12.44	13.21	0.77	0.72	0.279
40	-	23.91	23.17	0.72	1.35	0.524	19.63	19.88	0.64	1.18	1.008	13.27	13.80	0.67	0.58	0.625
50	-	25.12	26.02	1.21	2.10	0.642	23.2	25.33	1.59	1.78	0.726	-	-	-	-	-
5	40 mm	0.96	1.47	0.36	0.54	0.261	-1.17	-0.51	0.60	0.37	0.334	1.21	0.98	0.25	0.12	0.154
5	80 mm	10.89	10.65	0.72	0.77	0.380	6.75	6.10	0.68	0.62	0.437	9.02	8.13	0.70	0.59	0.403
5	40 & 80 mm	8.42	7.68	0.74	0.65	0.332	4.44	4.28	0.51	0.92	0.306	5.85	5.62	0.45	0.60	0.271

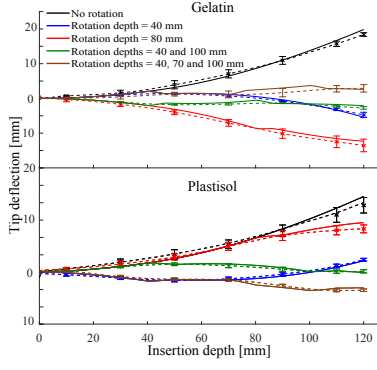


Fig. 9. A comparison of experimentally-obtained needle tip deflections and the corresponding model predictions for needle insertion using a flexible Nitinol wire at a constant insertion velocity of 5 mm/sec with and without axial rotation in gelatin and plastisol. Solid and dashed lines denote model prediction and experimental data, respectively.

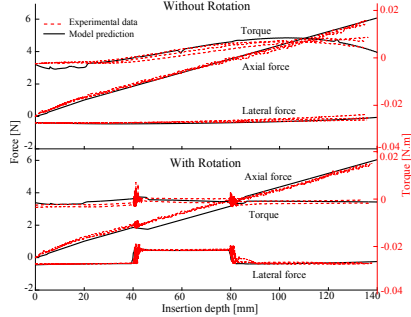


Fig. 10. A comparison of experimentally-obtained needle base forces and torque and the corresponding model predictions for needle insertion in plastisol at constant insertion velocity of 5mm/sec with no axial rotation and with double rotation at depths of 40 and 80 mm

the same using the developed carrier model given by (14). Based on results the model accurately captures the effect of needle deflection on axial and lateral needle base forces. Maximum RMSEs between model predictions and average experimental value of axial and lateral forces are 0.185 N and 0.073 N, respectively, for the insertion with double rotation. Maximum RMSE of model prediction for torque is 0.009 N.m for the insertion with single rotation.

As a part of model simplification discussed in II-C, we replaced the infinite-dimensional continuous model of needle dynamics by a discrete model using the assumed-modes method. In this method, the PDE used in modeling the needle deflection is approximated by a linear combination of four arbitrarily assumed shape modes representing the first four modes of needle vibration. Increasing the number of modes can enhance the accuracy of discretization method. However, it will also increase the model complexity, thus making the model computationally inefficient for real-time control purposes. Let us investigate the trade-off between the computational efficiency and the prediction accuracy of

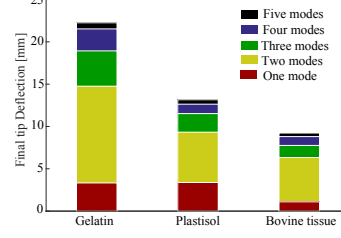


Fig. 11. Model prediction of final tip deflection at insertion depth of 140 mm and constant insertion velocity of 5 mm/sec for different number of assumed modes.

TABLE IV
COMPARISON OF EXPERIMENTAL DATA AND KINEMATICS-BASED MODEL PREDICTION.

	Gelatin			Plastisol		
	$\omega_{sim}(\ell)$ [mm]	e_{max} [mm]	RMSE [mm]	$\omega_{sim}(\ell)$ [mm]	e_{max} [mm]	RMSE [mm]
V=5 [mm/sec]	19.7	1.28	0.527	14.03	0.61	0.841
V=20 [mm/sec]	19.7	1.49	0.738	14.03	2.72	0.987
V=40 [mm/sec]	19.7	3.72	1.067	14.03	7.68	1.201
Rotation at 40 mm	4.5	2.86	1.505	-1.7	0.53	0.782
Rotation at 80 mm	10.8	0.36	1.327	5.24	1.81	1.208
Rotations at 40 & 80 mm	9.8	1.63	0.912	4.30	0.72	0.822

the model. Fig. 11 shows model prediction of the final tip deflection at an insertion depth of 140 mm and for a constant insertion velocity of 5 mm/sec in three tissues for different numbers of assumed modes. Based on the results, needle tip deflection accuracy initially increases as we increase the number of modes. However, after the 4th mode, the change in the final tip deflection is less than 1 mm – a maximum of 0.756 mm for gelatin and minimum of 0.24 mm for bovine tissue. Thus increasing the number of assumed modes any further is not necessary. We were able to solve the 4-mode model on an Intel Core i7 (2.93 GHz) machine with 4 GB memory at a sampling frequency of 10 kHz in a total computation time of 0.28 sec. A comparison of model accuracy and total computation time for solving the system of ODEs representing the model proves that four assumed modes are sufficient for developing an accurate model that can be used in control of needle steering.

Finally, we compare the accuracy of our model with the kinematics-based bicycle model [3]. The bicycle model is more general than the unicycle model [8] and can be reduced to a one-parameter unicycle model by fixing one of its parameters. For the sake of comparison, we have only used the kinematics-based model as it is reported to have better accuracy [3]. Needle insertions are performed with axial rotation(s) at constant velocity of 5 mm/sec and without axial rotation at constant velocities of 5, 20 and 40 mm/sec. Table IV presents a comparison of experimental data and kinematics-based model predictions. Fig. 12 shows a comparison of kinematics-based model predictions with experimentally-obtained needle tip deflections for needle insertion at a constant velocity of 5 mm/sec with and without axial rotation. The model parameters are identified as proposed in [3].

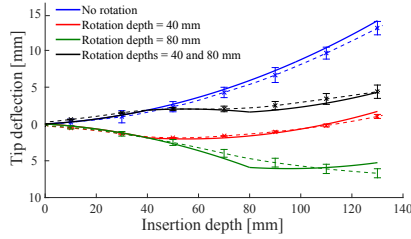


Fig. 12. A comparison of kinematics-based model predictions and experimentally-obtained needle tip deflections for needle insertion at a constant velocity of 5 mm/sec with and without axial rotation in plastisol. Solid and dashed lines denote model prediction and experimental data, respectively.

Compared to our model, the kinematics-based model shows a similar fit to experimental data for fixed insertion velocity of 5 mm/sec and with no rotation. However, the model's accuracy decreases when the needle is axially rotated. This is partly because it fits the model parameters empirically for every experimental condition (e.g., every constant insertion velocity and depth of rotation) while our model requires only one global parameter fit. Also, one of the main assumptions of the bicycle model is that the needle is flexible relative to the tissue, meaning that it can be steered without causing large tissue deformations. Thus, the model has been widely used for steering of flexible wires in soft tissues. However, when applied to path planning and control in softer tissues using standard brachytherapy needles, which are three times stiffer than a Nitinol wire, there is significant error in the kinematic model predictions. Compared to the kinematic model, the proposed model demonstrates good accuracy in both soft material and stiff material for both wire and needle. Lastly, compared to the kinematic model, the proposed model accepts as input a *variable* insertion velocity. According to the results given in Table IV, the kinematics-based model's accuracy decreases as insertion velocity is increased. This is mainly due to the fact that the model considers a constant velocity-independent radius of curvature for the needle tip trajectory and neglects the effects of tissue stiffness, friction and velocity dependent cutting force on tip deflection.

In order to improve the performance of the model for predicting needle deflection in multilayer heterogeneous tissue we plan to study the effects of tissue inhomogeneity on needle/tissue interaction forces more accurately in future. However, in the proposed model we can select different parameters for needle/tissue interaction models to simulate different layers of tissue. In the future, we intend to use the 2D model for controlled needle steering. In most of the needle-based medical interventions such as brachytherapy the goal is to insert the needle on a straight line and a grid template is used to position the needle in a fixed insertion plane that contains the target. Thus, the 2D model can be used to control the in plane deflection via 180° axial rotations of the needle. We will also extend the model to 3D to simulate full needle rotation and control the out of plane needle deflection. Extending 2D beam models to estimate 3D deflection has been studied previously [35]. The vectorial format used to derive the kinematic and dynamic equations makes this process easier. The proposed methodology used to model needle/tissue interaction forces as external excitation forces allows one to implement the interaction force models in the 3D model. Also, We plan to implement the model in a robotics-assisted needle steering scheme. Fully-robotic needle insertion has

been widely researched in the literature. In fully robotic needle steering the goal is to calculate a needle steering control input (mainly needle axial rotation) assuming the rest are fixed at known values such that needle targeting accuracy is improved [14], [15]. A possible intermediate step between fully-manual and fully-robotic insertion is semi-manual needle insertion, in which automatic robot-assisted adjustments are performed to one of the control inputs while other inputs are directly applied by the surgeon. For instance, the surgeon is left in charge needle insertion in the interest of ensuring the safety of operation and continuous engagement of the surgeon, while the needle tip bevel location is controlled robotically. The proposed model can be used for the semi-manual insertion as it responds to all the needle steering inputs (i.e., axial rotation, insertion velocity, needle base force/torque), only over some of which there is robotic control.

V. CONCLUDING REMARKS

In this paper, a novel approach is used to develop a dynamic model of needle steering in soft tissue. The model relates needle deflection to insertion velocity and axial rotation of the needle, which can be regarded as control inputs for needle steering. By means of a novel *time-delayed* tissue model embedded in the proposed model the needle tip position is accurately predicted. Also, the model is computationally efficient and allows for real-time control of the needle tip position in a robotic-assisted needle insertion context. Needle insertion experiments are performed at different velocities with axial rotation(s) at different insertion depths on synthetic and ex-vivo animal tissue with a needle-driving robot and using two different needles to identify the model parameters and validate the needle steering model. In the collected experimental data, the maximum error of the 2D model in predicting the needle tip position in the insertion plane was 1.59 mm in case of no axial rotation and 0.74 mm with axial rotation. The results confirm the model's accuracy and capability in capturing the effects of insertion velocity and axial needle rotation on needle deflection, thus enabling future applications in pre-surgery motion planning, optimized trajectory design and real-time control of needle steering.

ACKNOWLEDGEMENTS

This work was supported by the Natural Sciences and Engineering Research Council (NSERC) of Canada under grant CHRP 446520, the Canadian Institutes of Health Research (CIHR) under grant CPG 127768 and the Alberta Innovates - Health Solutions (AIHS) under grant CRIO 201201232.

REFERENCES

- [1] J. Swensen, M. Lin, A. Okamura, and N. Cowan, "Torsional dynamics of steerable needles: Modeling and fluoroscopic guidance," *IEEE Transactions on Biomedical Engineering*, vol. 61, no. 11, pp. 2707–2717, Nov 2014.
- [2] S. Misra, K. Reed, B. Schafer, K. Ramesh, and A. Okamura, "Mechanics of flexible needles robotically steered through soft tissue," *Int. J. Rob. Res.*, vol. 29, no. 13, pp. 1640–1660, 2010.
- [3] R. Webster, N. Cowan, G. Chirikjian, and A. Okamura, "Nonholonomic modeling of needle steering," in *Experimental Robotics IX*. Springer Berlin Heidelberg, 2006, vol. 21, pp. 35–44.
- [4] S. DiMaio and S. Salcudean, "Needle steering and model-based trajectory planning," in *Medical Image Computing and Computer-Assisted Intervention - MICCAI 2003*. Springer Berlin Heidelberg, 2003, vol. 2878, pp. 33–40.
- [5] O. Goksel, S. Salcudean, and S. Dimai, "3D simulation of needle-tissue interaction with application to prostate brachytherapy," *Computer Aided Surgery*, vol. 6, pp. 279–88, 2006.

- [6] R. Alterovitz, A. Lim, K. Goldberg, G. Chirikjian, and A. Okamura, "Steering flexible needles under Markov motion uncertainty," in *IEEE/RSJ International Conference on Intelligent Robots and Systems*, 2005, pp. 1570–1575.
- [7] N. Chentanez, R. Alterovitz, D. Ritchie, L. Cho, K. K. Hauser, K. Goldberg, J. R. Shewchuk, and J. F. O'Brien, "Interactive simulation of surgical needle insertion and steering," in *ACM SIGGRAPH 2009 papers*. ACM, 2009, pp. 1–10.
- [8] W. Park, J. S. Kim, Y. Zhou, N. Cowan, A. Okamura, and G. Chirikjian, "Diffusion-based motion planning for a nonholonomic flexible needle model," in *Robotics and Automation, 2005. ICRA 2005. Proceedings of the 2005 IEEE International Conference on*, 18–22 April 2005, pp. 4600–4605.
- [9] K. Yan, W. S. Ng, K.-V. Ling, Y. Yu, T. Podder, T.-I. Liu, and C. W. S. Cheng, "Needle steering modeling and analysis using unconstrained modal analysis," in *The First IEEE International Conference on Biomedical Robotics and Biomechatronics*, 2006, pp. 87–92.
- [10] O. Goksel, E. Dehghan, and S. E. Salcudean, "Modeling and simulation of flexible needles," *Medical Engineering & Physics*, vol. 31, no. 9, pp. 1069 – 1078, 2009.
- [11] R. Roesthuis, M. Abayazid, and S. Misra, "Mechanics-based model for predicting in-plane needle deflection with multiple bends," in *4th IEEE RAS EMBS International Conference on Biomedical Robotics and Biomechatronics*, 2012, pp. 69–74.
- [12] M. Khadem, B. Fallahi, C. Rossa, R. Sloboda, N. Usmani, and M. Tavakoli, "A mechanics-based model for simulation and control of flexible needle insertion in soft tissue," in *IEEE International Conference on Robotics and Automation (ICRA)*, 2015.
- [13] K. Reed, A. Okamura, and N. Cowan, "Modeling and control of needles with torsional friction," *IEEE Transactions on Biomedical Engineering*, vol. 56, no. 12, pp. 2905–2916, Dec 2009.
- [14] G. J. Vrooijink, M. Abayazid, S. Patil, R. Alterovitz, and S. Misra, "Needle path planning and steering in a three-dimensional non-static environment using two-dimensional ultrasound images," *The International Journal of Robotics Research*, 2014.
- [15] S. Patil, J. Burgner, R. Webster, and R. Alterovitz, "Needle steering in 3D via rapid replanning," *IEEE Transactions on Robotics*, vol. 30, no. 4, pp. 853–864, Aug 2014.
- [16] P. Moreira and S. Misra, "Biomechanics-based curvature estimation for ultrasound-guided flexible needle steering in biological tissues," pp. 1–11, 2014.
- [17] K. Reed, V. Kallem, R. Alterovitz, K. Goldberg, A. Okamura, and N. Cowan, "Integrated planning and image-guided control for planar needle steering," in *2nd IEEE RAS & EMBS International Conference on Biomedical Robotics and Biomechatronics, BioRob*, 2008, pp. 819–824.
- [18] P. Hagedorn and A. DasGupta, *Vibrations and Waves in Continuous Mechanical Systems*. Wiley, 2007, pp. 113–120.
- [19] L. Meirovitch, "Derivation of equations for flexible multibody systems in terms of quasi-coordinates from the extended hamilton's principle," *Shock and Vibration*, vol. 1, no. 2, pp. 107–119, 1993.
- [20] B. Galerkin, "Series solution of some problems of elastic equilibrium of rods and plates," *Wjestrnik Ingenerow Petrograd*, pp. 897–908, 1915.
- [21] G. Genta, *Vibration Dynamics and Control*. Springer, 2009, pp. 280–306.
- [22] A. Asadian, R. Patel, and M. Kermani, "Dynamics of translational friction in needle tissue interaction during needle insertion," *Annals of Biomedical Engineering*, vol. 42, no. 1, pp. 73–85, 2014.
- [23] A. M. Okamura, C. Simone, and M. D. O'Leary, "Force Modeling for Needle Insertion into Soft Tissue," *IEEE Transactions on Biomedical Engineering*, vol. 51, pp. 1707–1716, 2004.
- [24] S. Misra, K. Reed, A. Douglas, K. Ramesh, and A. Okamura, "Needle-tissue interaction forces for bevel-tip steerable needles," in *2nd IEEE RAS & EMBS International Conference on Biomedical Robotics and Biomechatronics(BioRob)*, 2008, pp. 224–231.
- [25] M. Mahvash and P. Dupont, "Mechanics of dynamic needle insertion into a biological material," *IEEE Transactions on Biomedical Engineering*, vol. 57, no. 4, pp. 934–943, 2010.
- [26] T. Anderson, *Fracture Mechanics: Fundamentals and Applications, Third Edition*. Taylor & Francis, 2005.
- [27] T. Podder, D. Clark, D. Fuller, J. Sherman, and et.al., "Effects of velocity modulation during surgical needle insertion," in *27th Annual International Conference of the Engineering in Medicine and Biology Society, IEEE-EMBS*, 2005, pp. 5766–5770.
- [28] S. Li and A. Oldenburg, "Measuring soft tissue elasticity by monitoring surface acoustic waves using image plane digital holography," in *Society of Photo-Optical Instrumentation Engineers (SPIE) Conference Series*, vol. 2, Mar. 2011, p. 7965.
- [29] K. Youcef-Toumi and O. Ito, "A time delay controller for systems with unknown dynamics," in *American Control Conference, 1988*, 15–17 June 1988, pp. 904–913.
- [30] A. Choi and Y. Zheng, "Estimation of Young's modulus and Poisson's ratio of soft tissue from indentation using two different-sized indentors: Finite element analysis of the finite deformation effect," *Medical and Biological Engineering and Computing*, vol. 43, no. 2, pp. 258–264, 2005.
- [31] M. Kermani, R. Patel, and M. Moallem, "Friction identification and compensation in robotic manipulators," *IEEE Transactions on Instrumentation and Measurement*, vol. 56, no. 6, pp. 2346–2353, 2007.
- [32] T. Johnson and P. Husbands, "System identification using genetic algorithms," in *Parallel Problem Solving from Nature*. Springer Berlin Heidelberg, 1991, vol. 496, pp. 85–89.
- [33] M. Waine, C. Rossa, R. Sloboda, N. Usmani, and M. Tavakol, "3d needle shape estimation in trus-guided prostate brachytherapy using 2d ultrasound images," *IEEE Journal of Biomedical and Health Informatics*, 2015, In press.
- [34] T. Podder, J. Sherman, D. Clark, and et.al., "Evaluation of robotic needle insertion in conjunction with in vivo manual insertion in the operating room," in *Robot and Human Interactive Communication, 2005. ROMAN 2005. IEEE International Workshop on*, 13–15 Aug. 2005, pp. 66–72.
- [35] L. Merovitch and T. Stemple, "Hybrid equations of motion for flexible multibody systems using quasi-coordinates," in *Guidance, Navigation, and Control and Co-located Conferences*. American Institute of Aeronautics and Astronautics, 1993.



Mohsen Khadem received his BSc and MSc degrees in mechanical engineering from Shiraz University and Sharif University of Technology, Iran, in 2010 and 2013, respectively. He is currently working towards the Doctoral degree in Electrical and Computer Engineering at University of Alberta and is working on robotics-assisted minimally invasive surgery. His current research interests include medical robotics and image-guided surgery.



Carlos Rossa received the Engineering and the M.Sc degrees in Mechatronics from the Ecole Nationale d'Ingenieurs de Metz, France, both in 2010, and earned the PhD degree in Mechatronics and Robotics from the University of Paris VI, France in 2013. He is currently a postdoctoral research fellow with the Department of Electrical and Computer Engineering at the University of Alberta, Canada. Dr. Rossa's current research interests include the design and control of haptic interfaces, actuators and sensors technologies, mechatronics, and medical robotics.



Nawaid Usmani is an Associate Professor in Department of Oncology, University of Alberta, and a radiation Oncologist at Cross Cancer Institute, Canada. He received Bachelor of Arts & Science from McMaster University, Canada in 1998 and Doctorate of Medicine from McMaster University in 2001. Dr. Usmani's main focus on research is in prostate brachytherapy, including MRI and PET imaging in management of prostate cancer.



Ron S. Sloboda is a Professor in Department of Oncology, University of Alberta, Canada. He received BSc degree in Physics from the University of Manitoba, Canada, in 1974 and PhD degree in Physics, Nuclear Theory from the University of Alberta, Canada, in 1979. Dr. Sloboda's research interests are dosimetry and treatment planning for brachytherapy, including the design of clinical studies to obtain patient data and model-based dose calculation.



Mahdi Tavakoli is an Associate Professor in the Department of Electrical and Computer Engineering, University of Alberta, Canada. He received his BSc and MSc degrees in Electrical Engineering from Ferdowsi University and K.N. Toosi University, Iran, in 1996 and 1999, respectively. He received his PhD degree in Electrical and Computer Engineering from the University of Western Ontario, Canada, in 2005. In 2006, he was a post-doctoral researcher at Canadian Surgical Technologies and Advanced Robotics (CSTAR), Canada. In 2007–2008, he was an NSERC Post-Doctoral Fellow at Harvard University, USA. His research interests broadly involve the areas of robotics and systems control. Specifically, his research focuses on haptics and teleoperation control, medical robotics, and image-guided surgery.